Research Article | Vol. 31, No. 13 / 19 Jun 2023 / Optics Express 21128
Optics EXPRESS

# Modeling sea ice albedo and transmittance measurements with a fully-coupled radiative transfer model

ZHONGHAI JIN,[1,*] MATTEO OTTAVIANI,[1,2] AND MONIKA SIKAND[1,3,4]

[1]NASA Goddard Institute for Space Studies, New York, NY, USA
[2]Terra Research, Hoboken, NJ, USA
[3]Department of Applied Physics and Applied Mathematics, Columbia University, New York, NY, USA
[4]Now at Department of Physics, Stevens Institute of Technology, Hoboken, NJ, USA
[*]zhonghai.jin@nasa.gov

**Abstract:** A rigorous treatment of the sea ice medium has been incorporated in the advanced Coupled Ocean-Atmosphere Radiative Transfer (COART) model. The inherent optical properties (IOPs) of brine pockets and air bubbles over the 0.25-4.0 μm spectral region are parameterized as a function of the sea ice physical properties (temperature, salinity and density). We then test the performance of the upgraded COART model using three physically-based modeling approaches to simulate the spectral albedo and transmittance of sea ice, and compare them with measurements collected during the Impacts of Climate on the Ecosystems and Chemistry of the Arctic Pacific Environment (ICESCAPE) and the Surface Heat Budget of the Arctic Ocean (SHEBA) field campaigns. The observations are adequately simulated when at least three layers are used to represent bare ice, including a thin surface scattering layer (SSL), and two layers to represent ponded ice. Treating the SSL as a low-density ice layer yields better model-observation agreement than treating it as a snow-like layer. Sensitivity results indicate that air volume (which determines the ice density) has the largest impact on the simulated fluxes. The vertical profile of density drives the optical properties but available measurements are scarce. The approach where the scattering coefficient for the bubbles is inferred in lieu of density leads to essentially equivalent modeling results. For ponded ice, the albedo and transmittance in the visible are mainly determined by the optical properties of the ice underlying the water layer. Possible contamination from light-absorbing impurities, such as black carbon or ice algae, is also implemented in the model and is able to effectively reduce the albedo and transmittance in the visible spectrum to further improve the model-observation agreement.

© 2023 Optica Publishing Group under the terms of the Optica Open Access Publishing Agreement

## 1. Introduction

Sea ice is a vital component of the global climate system, since it affects heat and moisture exchange within the atmosphere and ocean, and strongly impacts the surface energy budget [1–4]. A reduction in sea ice cover and its thinning lower the albedo and increases shortwave absorption in the ocean, causing more melting in a mechanism known as ice-albedo feedback [5–8], which has been quantified as the second main contributor to the Arctic amplification using climate simulations [9,10]. Many sea ice models employ simplistic parameterizations for the albedo, and typically neglect its dependence on ice physical properties such as salinity, density and their vertical distribution. Such an approach can lead to unrealistic estimates of albedo and transmittance, and therefore to large uncertainties in both present-day simulations and future climate projections in the Arctic [11–14].

An accurate description of the interaction between sea ice and solar radiation requires adequate estimations of the multiple scattering processes and the absorption rate within the ice column.

#491306 https://doi.org/10.1364/OE.491306
Journal © 2023 Received 24 Mar 2023; revised 21 May 2023; accepted 23 May 2023; published 8 Jun 2023

Optics EXPRESS

To improve our confidence in model projections of sea ice extent and thickness, it is therefore crucial to develop accurate and efficient radiative transfer models. A detailed characterization of the optical behavior of sea ice is even more important since the latter changes dramatically in response to structural variations, as a freezing water surface grows into a stable pack, to then age and undergo possible melting [15–18]. The first stages of sea-ice formation are associated with the phase transition, and are characterized by increasing salinity, viscosity and elasticity [19,20]. "Young ice" of a thickness up to 30 cm, that can still be fractured by wave motion, evolves eventually into more stable first-year ice (FYI) with thicknesses up to 2 m [21]. If FYI survives the melting season, it ages into multi-year ice (MYI) which typically exhibits a moderate increase in thickness (for a total thickness of 2-4 m), and a decrease in density and salinity mainly caused by an increase of air volume and the flushing of brine [22–24]. If a bare MYI surface is exposed, it commonly exhibits a blue tint because bubbles act as scattering centers. The reported values of sea ice density, at least for the bulk of the ice, vary over a wide range, from 0.72 g/cm$^3$ to 0.94 g/cm$^3$ [25].

The springtime increase in ambient temperature can trigger the formation of water ponds on top of the sea ice surface [26]. Compared to white, bare ice, the albedo of ponded ice can be reduced dramatically across all shortwave wavelengths, while remaining fairly constant in the infrared because of the strong absorption of water [27]. Melt ponds occur in late spring and summer, when solar irradiance is largest. Because water reflects much less and transmits much more than ice, melt ponds can therefore alter significantly the solar energy distribution in the atmosphere-sea ice-ocean system.

Spectral observations are required for an accurate determination of the attenuation of solar radiation in sea ice. Field and remote sensing measurements of the spectral albedo, spectral transmittance, and extinction coefficients have been reported for a variety of the ice types mentioned above [28–35]. Among these studies, the two from Light et al. [28,29] are particularly relevant to our analyses, and for brevity will hereafter be referred to as L08 and L15, respectively. However, simultaneous observations of entire vertical columns in the cryosphere, including vertical profiles of the sea ice physical properties, have traditionally been sparse. Notable field campaigns include the First International Satellite Cloud Climatology Project (ISCCP) Regional Experiment (FIRE) Arctic Clouds Experiment (FIRE ACE [36]), the Surface Heat Budget of the Arctic Ocean (SHEBA [31]), and the Impacts of Climate on the Ecosystems and Chemistry of the Arctic Pacific Environment (ICESCAPE, L15). Fortunately, large campaigns such as the recently concluded Multidisciplinary drifting Observatory for the Study of Arctic Climate (MOSAiC [37]) and the planned Arctic Radiation-Cloud-Aerosol-Surface Interaction Experiment (ARCSIX [38]) will provide comprehensive datasets to complement the observations from SHEBA and ICESCAPE with increased instrumentation and technological capabilities.

Radiation measurements as those collected in the campaigns listed above are critical for the validation of radiative transfer models. Efforts to simulate sea-ice albedo and transmittance measurements are reported in a few dedicated studies. Grenfell [39] employed a four-stream, discrete-ordinate radiative transfer code to investigate light propagation within sea ice, a model thereafter used by L08 and L15. Briegleb and Light [40] employed the Delta-Eddington scheme in a climate model. Jin et al. [41] developed a broadband multiple-stream, coupled radiative transfer model to investigate the solar radiation distribution and absorption in the polar atmosphere, sea ice and ocean system. This model was also used by Hamre et al. [42] to study short-wave transmission through first-year thin ice. Taskjelle et al. [35] applied the derivative AccuRT software [43] to retrieve the properties of newly formed (very thin) ice. Many sea ice radiative transfer models require the Inherent Optical Properties (IOPs) at input, which constitutes a major limitation since the IOPs are very challenging to measure *in situ* and even in laboratory. As a consequence, the IOPs more or less always suffer from very significant approximations. For example, L08, L15 and Briegleb and Light [40] use a constant, spectrally-flat scattering

Optics EXPRESS

asymmetry factor of 0.94 and the derived or fixed scattering coefficients, while Lamare et al. [44] use a scattering asymmetry factor of 0.98 and constant scattering coefficients. Light et al. [45] developed a model for FYI, where brine and gas size distributions are used to parameterize the IOPs in lieu of density, and the treatments of brine and gas scattering are based on the approximate similarity principle.

Extending the analysis to the modeling of melt ponds, which add a further element of complexity deeply affecting the radiative balance in the melting season [46–48], Zege et al. [49] have developed a detection algorithm capable to produce the spectral albedo of melt ponds based on multispectral satellite observations.

Meeting the modeling needs described above requires a tool capable of rigorously calculating the radiative distribution in the atmosphere-sea ice-ocean system. As described in the next section, Jin et al. [50] developed a Coupled Ocean-Atmospheric Radiative Transfer (COART) model with high spectral resolution (up to 0.1 $cm^{-1}$) to accurately account for atmospheric absorption, and adequate treatment of surface roughness. Here, this previously validated [51,52] COART model is extended to include the sea ice medium. The sea ice optical properties are directly parameterized as a function of its measurable physical properties (i.e., temperature, salinity, and density), so as to eliminate the need to provide the IOPs (extinction, single scattering albedo, and asymmetry factor) at input. The rest of the ocean/atmospheric column can accommodate any species whose IOPs are known. This physically-based strategy also enables a direct connection with the physical ice properties simulated in climate models.

The objective of this study is to test the stated parameterization and evaluate different modeling approaches against observations of albedo and transmittance by constraining the physical properties with measurements of their vertical profiles whenever available. The augmented COART model is described in Sec. 2. Different modeling approaches are introduced and evaluated against ICESCAPE and SHEBA measurements of spectral albedo and transmittance in Sec. 3, including sensitivity studies with respect to light-absorbing impurities. The ice types include bare and ponded sea ice in the melting season (the presence of snow is not a focus of the present study, although it can be accounted for by the model). The conclusions are presented in Sec. 4. The Appendix provides additional sensitivity tests.

## 2. Radiative transfer model

The radiative transfer model used in this study is developed from COART [50], a multiple scattering code for the coupled atmosphere-ocean system based on the discrete-ordinate DISORT algorithm [53] but modified to account for the change in refractive index across the air-water interface. The atmosphere and the ocean each can be divided into an arbitrary number of layers, in order to resolve the vertical variation of physical properties. Treatment of absorption and multiple scattering by gasses, aerosols, and clouds in the atmosphere and CDOM, phytoplankton and non-plankton particulates in the ocean is included. The atmospheric absorption database is adopted from the MODTRAN code and has different available spectral resolutions up to 0.1 $cm^{-1}$ [54].

The ice medium has now been implemented for applications to the cryosphere, with spectral refractive index from Warren and Brandt [55]. Since reflection and refraction processes due to the change in refractive index across the air-ice-water interfaces are rigorously taken into account when solving the radiative transfer equation, radiative processes in the coupled atmosphere-sea ice-ocean system are treated consistently and efficiently. The ocean and ice layers are treated in the same way as the atmospheric layers, but with significantly different optical properties. The same Gaussian normal distribution used to model the ocean surface roughness [56] is also used to describe the slope distribution of the facets forming the ice surface. The surface roughness reduces the surface albedo because of shadowing, but this effect is non-negligible only for grazing directions of the incident light. The possible occurrence of melt ponds on top of the ice is

Optics EXPRESS

also considered, in the form of a pure freshwater layer of any desired depth. Water absorption data is from the compilation of Pope and Fry [57] and Smith and Baker [58]. Since COART has previously been validated for radiation studies in the atmosphere and ocean [51,52], in this study we focus on evaluating the performance of the newly implemented model in simulating the radiation field reflected and transmitted by the sea ice medium.

Absorption by pure ice, and scattering and absorption by brine pockets and air bubbles enclosed in the ice are at the base of the treatment. The total ice layer absorption is the average of ice and brine water weighted by volume fractions. In addition to the absorption by pure ice, and the scattering and absorption by brine pockets and air bubbles, the presence of other possible inclusions such as black carbon (BC) and phytoplankton can also be considered. The addition of other scattering and absorbing particulates is trivial and can be achieved via the compilation of tabulated IOPs. The ice absorption coefficient is also based on the compilation of Warren and Brandt [55]. Based on the phase equilibrium constraints, the total brine and air volumes are determined by the ice temperature, salinity and density [59]. The inherent optical properties (IOPs) of bubbles are obtained with Mie calculations, using a power-law size distribution [45,60–62]. Following Light et al. [60], the bubble number distribution, $N(r_{bub})$, is represented as a function of bubble equivalent radius ($r_{bub}$) as:

$$N(r_{bub}) = N_0\, r_{bub}^{-1.5} \tag{1}$$

where $N_0$ is determined by total air volume calculated through the Eq. (14) of Cox and Weeks [59], that is:

$$V_{air} = \frac{4}{3}\pi \int_{r_{min}}^{r_{max}} N\,(r_{bub})\; r_{bub}^3\, dr_{bub} \tag{2}$$

The minimum and maximum bubble radii are set to 0.01 mm and 1.0 mm, respectively, approximately the range observed [60,61]. The horizontal cross-sectional area of brine inclusions can also be fitted by a power-law distribution [60,63]. Using the effective radius of equivalent spheres ($r_{bri}$) with the same area distribution as in Light et al. [60], the size distribution of brine pockets is given by the following power-law relation:

$$N(r_{bri}) = N_0\, r_{bri}^{-2.73} \tag{3}$$

As for the air bubbles (Eq. (2)), the total brine number is determined by the total brine volume calculated from Eqs. (4) and (5) in Cox and Weeks [59] but with the size distribution defined by Eq. (3). The size range of the brine pockets is 0.01-0.15 mm.

Due to the large size parameter and the similar refractive indices of brine and ice in the shortwave part of the spectrum, most of the light scattered by brine is concentrated in a very small cone around the forward direction, which contains all the scattering by diffraction and most of the scattering component from refraction and transmission. This forward scattering peak can be considered as "non-scattered" and added back to the incident radiation in the radiative transfer algorithm. Therefore, the scattering coefficient can be scaled down dramatically, which essentially reduces the scattering efficiency of the brine pockets. The equivalent-sphere assumption may become problematic when brine size becomes large, but the forward scattering also becomes stronger as the size of the brine pockets increases. These factors make the error resulting from the uncertainties in brine size distribution and brine pocket shape much smaller than might be expected. On the other hand, air bubbles scatter much more effectively than brine pockets. Since the bubble sizes are significantly larger than the wavelength in the visible and near infrared, the spectral variation of the scattering efficiency for different size distributions is small. In addition, the asymmetry factor of air bubbles mainly varies with wavelength but not appreciably with the size distribution (see Fig. 1). Therefore, scaling the scattering coefficient of air bubbles by the same factor over all wavelengths is essentially equivalent to changing the bubble size

Optics EXPRESS

distribution, which provides a way to account for possible variations of the size distribution in different ice layers. As sea ice cools, solid salts may precipitate and be expelled from the brine pockets. However, the solid salt contribution only becomes significant at ice temperatures below the crystallization temperature of $NaCl{\cdot}2H_2O$ (−22.9°C). There is no size distribution reported for the salt; however, the cases studied here pertain to sea ice surveyed in the warm, summer season, so solid salt scattering can be neglected.

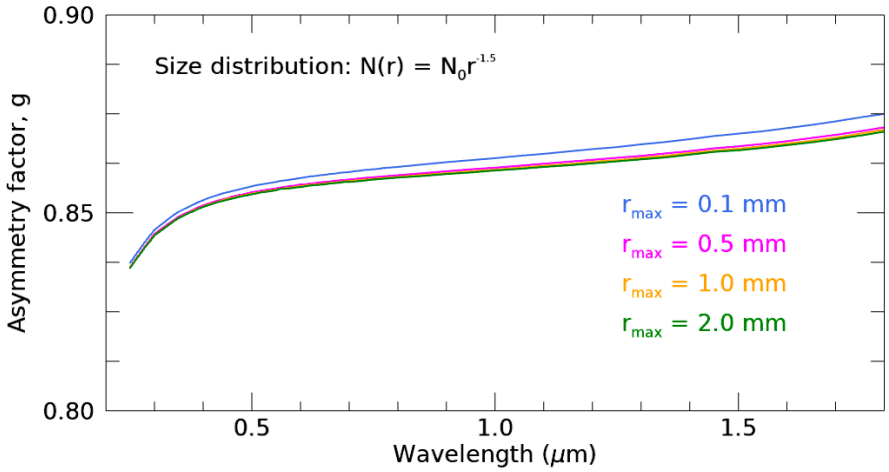


**Fig. 1.** Asymmetry factor as a function of wavelength for different bubble size distributions. Note the extremely small differences among the four curves.

Using the size distributions (Eqs. (1) and (3)), we generated look-up tables for the IOPs of brine pockets and air bubbles over the 0.25-4.0 µm spectral region. The sea ice IOPs are therefore directly associated with the ice physical properties, i.e., the temperature, salinity, and density, in turn used as the input parameters for the COART model. This physically-based approach provides a sophisticated and complete treatment of radiative transfer in sea ice. Beside the parameterization of brine pockets and air bubbles properties, the model is designed to easily adopt any other light-absorbing materials enclosed in the ice. We have currently included black-carbon aerosols [64] and ice algae [K. Arrigo, *personal comm.*].

## 3. Validation studies

### 3.1. Methodology

The spectral albedo and transmittance are Apparent Optical Properties (AOPs), which in the case of sea ice are mostly influenced by its physical structure and the angular distribution of the incident light, whereas the effects of atmospheric and oceanic particulates are less significant (except of course for very thin, optically-finite ice). If both are simultaneously fit with sufficient accuracy, it implies that the model correctly quantifies the total absorption in the ice column. For this reason, the spectral albedo and transmittance are frequently used in studies for understanding the radiative transfer in sea ice.

To model the Rayleigh background atmosphere, we use the standard subarctic atmosphere [65] to obtain the vertical profiles of pressure, temperature and density. For the ocean layers beneath the ice, the Chl-a concentration is set to 0.1 $mg/m^3$, about the average reported for the arctic ocean [66–68].

Optics EXPRESS

Because the ice IOPs are linked to the ice physical properties through the parametrization described in Sec. 2, the input parameters required by the radiative transfer model in the ice layers become simply the salinity, density and temperature. Together with the physical properties in the atmospheric and ocean layers, COART then calculates the irradiances at any desired level. The upwelling and downwelling irradiances at the ice surface and base are used to simulate the albedo and transmittance of sea ice for comparison with observations.

The comparison of MOSAiC and SHEBA observations in Light et al. [27] confirms that "the spectral albedo for bare, melting sea ice also appears invariant with respect to ice age (first year, second-year, multiyear)". The strong spectral dependence of the absorption coefficients for brine, ice, water and organic or other inclusions [15,63] is responsible for the nearly constant albedo in the visible region and the significant decrease in the near infrared region. To model the vertical structure of bare, melting sea ice, L08 and L15 utilize three layers corresponding to a granular, highly-scattering SSL, a denser drained layer (DL) and a high-density interior layer (IL). L08 identified the SSL, typically 1-5 cm thick, as having a significantly higher scattering coefficient than the ice layers beneath. The DL roughly occupies the remainder of ice sitting above the freeboard. The IL occupies the rest of the column beneath the DL and exhibits the lowest scattering coefficients. In order to determine the ice absorption, L08 set the ice density at 0.42, 0.83, and 0.92 g/cm$^3$ for the SSL, DL, and IL, respectively. The results of their simulations highlight that the optical properties of the SSL deeply affect the albedo (i.e., enhance it across all the spectrum, but especially in the near infrared), as confirmed by more recent studies [27,69]. To mirror this morphology and the input of L08 and L15, we also use a 3-layer structure in our modeling. For ponded ice, however, we use two ice layers with a water layer on top (Sec. 3.4).

For samples collected during the MOSAiC campaign, Macfarlane et al. [69] observe that "the SSL regenerates and maintains a consistent microstructural profile throughout the melt season". The reported average density is $0.332 \pm 0.084$ g/cm$^3$ in the top 2 cm and $0.579 \pm 0.109$ g/cm$^3$ in the lower 3 cm. Based on these observations, we set the thickness of the SSL to 5 cm, and subdivide it into a top sublayer (2 cm) with a density of 0.33 g/cm$^3$ and the bottom sublayer (3 cm) with a density of 0.60 g/cm$^3$. Despite this subdivision in density, we can still consider the SSL as a single layer since (i) an arbitrary number of sublayers can be used to resolve the density gradient in this layer of established physical nature; and (ii) salinity and temperature remain the same between the two sublayers (the gradient in temperature in such small thickness is negligible).

For the vertical profiles of the physical properties, we strived to use all available observational data, focusing on two common ice types: bare and ponded ice. When forced by the lack of *in-situ* observations, a density value within commonly accepted ranges is adopted as an initial guess, and then the density or the scaling factor for bubble scattering is inferred by using the measured albedo at one selected wavelength for one layer. The scaling factor at the selected wavelength is applied to the scattering coefficients of air bubbles at all other wavelengths. For the salinity profiles, in the case of ICESCAPE we use the exact values of layer-resolved salinity documented by Polashenski et al. [70] and partially in L15. Due to the lack of temperature profiles, we chose melting or ponded ice cases. For these cases, the temperature can be constrained based on fundamental physics: 0°C at the top of the ice layer because this is the coexisting temperature of water and ice, and −2°C at the bottom based on the freezing temperature of seawater. The temperature at any depth within the ice column is obtained by linear interpolation. Note that, as shown in the Appendix (Fig. 10), the sensitivity to temperature in this narrow range (0°C to −2°C) is small and therefore does not appreciably affect the quality of the fit. Plausible concentrations for chlorophyll and BC are only used for sensitivity tests, to demonstrate that the fit can be improved should measurements on these constituents be available (see Fig. 6).

Optics EXPRESS

Using the ice structure and properties described above as model input, we test three modeling approaches and evaluate their performance by comparison against the measured ICESCAPE and SHEBA spectral albedo and transmittance.

Within the first method (M1), the ice properties and the IOP parametrization described above are used to first calculate the spectral optical properties (i.e., scattering and absorption coefficients, and asymmetry factor) in each ice layer. Then, the scattering coefficient of the SSL is scaled so as to match the albedo measured at 1.35 µm, because the ice albedo at this wavelength is solely determined by the SSL properties. The resulting scaling factor is applied at all other wavelengths to characterize the bubble scattering component in the SSL. The albedo measured at 0.85 µm is similarly used to infer the bubble scattering component in the DL, because at this wavelength the albedo is determined by the SSL and DL but is unaffected by the IL. The inferred scaling factor is again applied to all wavelengths. The scaling factor for the IL is found in the same way by matching the albedo measured at 0.50 µm, which is impacted by all three layers. After the three scaling factors are applied, we calculate the spectral albedo and transmittance over the entire spectra. This scaling scheme is essentially equivalent to adjusting the bubble size distribution (practically unknown for the SSL and the DL), because the asymmetry factor for bubbles varies greatly with wavelength but little with size distribution (Fig. 1), whereas the scattering coefficient varies with size distribution but exhibits little change in spectral shape. The size distribution used for the bubble IOP parametrization is based on measured IL samples [60,61], and those in SSL and DL are likely to be different.

Within the second method (M2), we still infer and scale the scattering coefficients in the SSL and DL as done in M1, but for the IL we infer the ice density (by finding the value needed to match the albedo at 0.50 µm). As opposed to the scattering coefficient, the density does not depend on wavelength. Because the size distribution is based on measurements of the IL, this approach is equivalent to assuming that the size distribution in the IL is appropriately modeled, and that the inferred density corrects the total air volume or bubble concentration.

In M1 and M2, the SSL is considered as the same medium (ice) as the rest of the ice column, but with significantly lower bulk density. While we consider the SSL as an integral part of the ice column, a fairly good model-observation agreement in spectral albedo and transmittance is also obtained in L08 and L15 where the refractive index is assumed to change at the SSL–DL interface instead of the air-ice interface. This way, the SSL is effectively treated as a snow-like, granular ice layer, which has very different physical and optical properties from the rest of the ice column.

Although cases of snow over bare ice are not a focus of this paper, the augmented COART model can rigorously account for snow on top of the ice [71], and therefore we can evaluate the goodness of this assumption with a third modeling approach (M3) for the bare ice cases. Even though COART can handle different snow particle habits, to be consistent with L15 the snow is assumed to be composed of spherical grains. The albedo of an optically infinite snow layer is solely determined by the snow grain size [18,72]. Therefore, we infer this parameter as done in M1 and M2 by matching the albedo at a near-infrared wavelength, as opposed to inferring the scattering coefficient independently for each wavelength, which is unphysical.

### *3.2. Bare, first-year ice*

#### 3.2.1. Data

For bare FYI, we use data [73] from the ICESCAPE campaign, conducted in the Arctic Ocean between the Chukchi Sea and the Beaufort Sea regions.

The particular cases were selected because of optimal observational conditions and the most consistent set of measurements over best-defined bare sea ice, as per the field notes. The time and location (used to derive the Solar Zenith Angle, SZA, with a dedicated module of COART) and the total ice thickness are commonly reported. The illumination conditions were recorded

Optics EXPRESS

as "brilliantly clear" on 19 July, 2011 (SZA = 53°), and "completely overcast but with visible Sun" (SZA = 48°) on 3 July, 2010. As shown in the Appendix (Fig. 9), overcast conditions significantly affect the albedo only for very low or very high SZAs. The former never occur at extreme latitudes, and the SZA on 3 July, 2010 is within the 45°-60° range that allows to neglect the presence of clouds in the simulations.

A melting state and the presence of some ponds were reported for both these FYI surfaces along the "albedo line" connecting the collection sites, which extends to a length of 200 m. One observation on 3 July, 2010 was excluded since its very low average albedo in the visible (0.67) suggested the presence of an undetected thin water layer.

The total ice thickness, measured *in situ*, was 118 cm (averaged among the individual measurements of 103 cm, 115 cm and 135 cm) on 3 July, 2010, and 152 cm (averaged among 149 cm, 149 cm and 157 cm) on 19 July, 2011.

Density profiles from cores are generally very scarce. For ICESCAPE, they were available for the uppermost 80 cm of a core collected on 19 July, 2011 (see L15, Fig. 7), excluding the top 5 cm because of the destructive nature of the sampling technique. In this core section, the density was found to vary between 0.625 and 0.909 g/cm$^3$. The densities deeper into the ice were initialized at 0.85 g/cm$^3$ for the DL and 0.92 g/cm$^3$ for the IL, based on typical values for FYI reported by Timco and Frederking [25] (0.84-0.91 g/cm$^3$ for the ice above the waterline and 0.90-0.94 g/cm$^3$ for the ice below the waterline). The SSL density was constrained based on very recent observational data from MOSAiC [69], as described in Sec. 3.1.

For the salinity, we use the profiles reported from the core analyses of Polashenski et al. [70], averaging the available data points in each model layer. Since measurements are not reported for the SSL (which normally gets destroyed when collecting the cores) and considering the brine drainage (flushing) in this porous layer, we assume this layer is desalinated. This assumption seems reasonable in view of recent measurements, which indeed report very low values [74]. Moreover, our tests show no discernible differences in the modeled AOPs when the salinity varies between 0 and 1.0 ppt in the SSL. The salinity measurements are unavailable also for the lower portion of the IL, so we assume that the value at the lowest depth extends all the way to the bottom. For the three layers, the resulting salinity profiles were 0.0 (SSL), 0.42 (DL), 1.71 ppt (IL) on 3 July, 2010; and 0.0 (SSL), 0.59 (DL), 2.20 ppt (IL) on 19 July, 2011.

Polashenski et al. [70] report that the core temperatures were always between 0°C and −1°C. Such small variations in temperature have a negligible effect on the AOPs (see Fig. 10 in the Appendix). To facilitate the comparison among all simulations, and to be consistent with the expected temperature at the ice-ocean interface, we chose a linear temperature profile from 0°C at the surface to −2°C at the base.

#### 3.2.2. Results

Figure 2 compares the modeled and measured spectral albedo and transmittance for the two selected cases. The top panel is for 3 July, 2010, and the bottom panel for 19 July, 2011. The gray areas show the total range of each series of measurements. The albedo and transmittance modeled with method M1 are plotted as black lines. The scaling factors for the SSL are 0.30 (3 July, 2010) and 0.28 (19 July, 2011), indicating that the original sizes are too small for the bubbles in the SSL (a scaling factor smaller than 1.0 is equivalent to increasing the bubble sizes). Because of the complex relationships between ice optical and physical properties, as well as their dependence on wavelength (for example, the spectral variation of the asymmetry factor), a simultaneous fit to albedo and transmittance across all wavelengths would be completely accidental if the spectrally flat scaling approach of M1 were physically incorrect.

The spectral albedos obtained by applying method M2 almost overlaps, and only the transmittance in the upper panel shows slight differences. The retrieved ice density in the IL is 0.919 g/cm$^3$ for both cases. Although it remains challenging to simultaneously fit albedo and

Optics EXPRESS

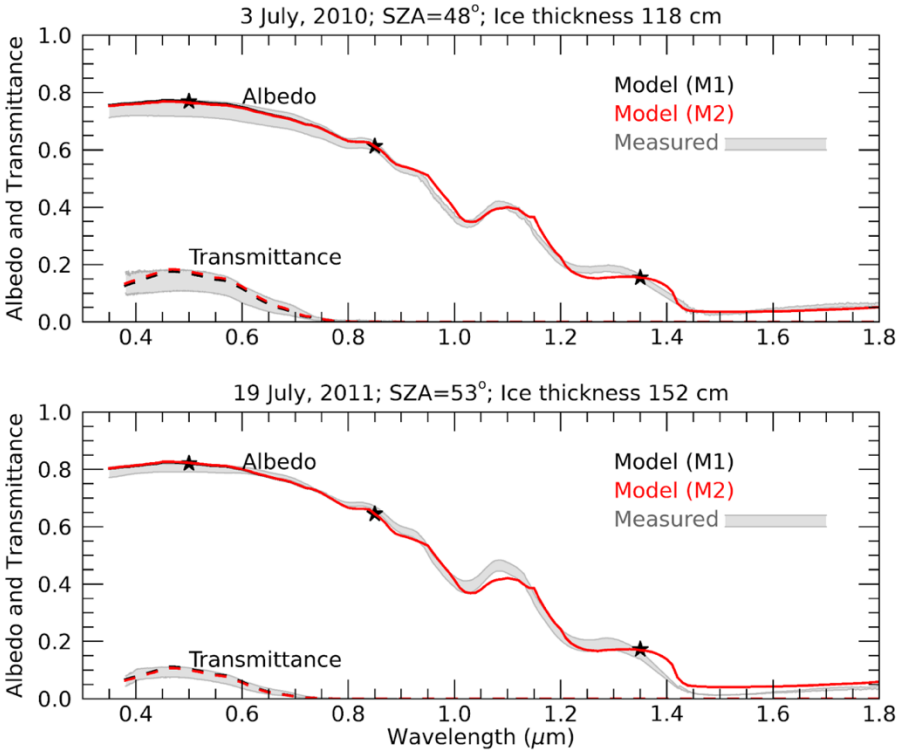


**Fig. 2.** Modeled spectral albedo and transmittance versus ICESCAPE observations of FYI (gray shaded areas), which took place in the Beaufort Sea on 3 July, 2010 (top panel, Station 68), and 19 July, 2011 (bottom panel, Station 129). The results of the M1 modeling approach that infers bubble scattering is shown in black, while the results of the M2 approach that infers the density of the interior layer is in red. The stars indicate the modeling albedo at the three selected wavelengths used to infer the ice properties.

transmittance in an optimal way in the absence of complete sets of measured density profiles, these results demonstrate how the augmented COART model correctly captures many of the spectral signatures of observed albedo and transmittance and their variations with the descriptive properties.

In the top panel of Fig. 3, we applied method M3 by substituting the ice SSL with a snow layer of equal density and thickness (5 cm). A snow effective radius $r_{eff}$ = 700 μm causes the albedo at 1.35 μm to fall within the observed range, but the agreement becomes very poor at all other wavelengths (black line). A snow layer of such thickness (5 cm) and density largely determines the albedo at most wavelengths; even in the visible spectrum the lower ice layers have only a minor effect. A snow grain size of $r_{eff}$ = 1500 μm leads to a match in albedo at 0.85 μm, but generally underestimate it at wavelengths >1.0 μm. However, the modeled transmittance (dashed lines) agrees well with measurements. To increase the impact of the underlying ice, the snow layer depth and/or density has to be reduced significantly. Therefore, in the lower panel, we reduced the snow layer depth to 3 cm and the density to 0.3 g/cm$^3$. Even for this thinned snow layer, we cannot successfully infer the bubble scattering (or ice densities) in the DL and IL required to simultaneously match the albedo at all three selected wavelengths, because of the strong attenuation of snow in the near infrared. A snow grain size of $r_{eff}$ = 700 μm leads to a match with the observed albedo at 1.35 and 0.50 μm but not at 0.85 μm (black line). Increasing the grain size to $r_{eff}$ = 900 μm can improve the overall agreement but underestimate the albedo at

Optics EXPRESS

wavelengths >1.2 µm (red line). To obtain better overall match, the snow depth or density must be further reduced to values that are unphysical to represent the SSL.

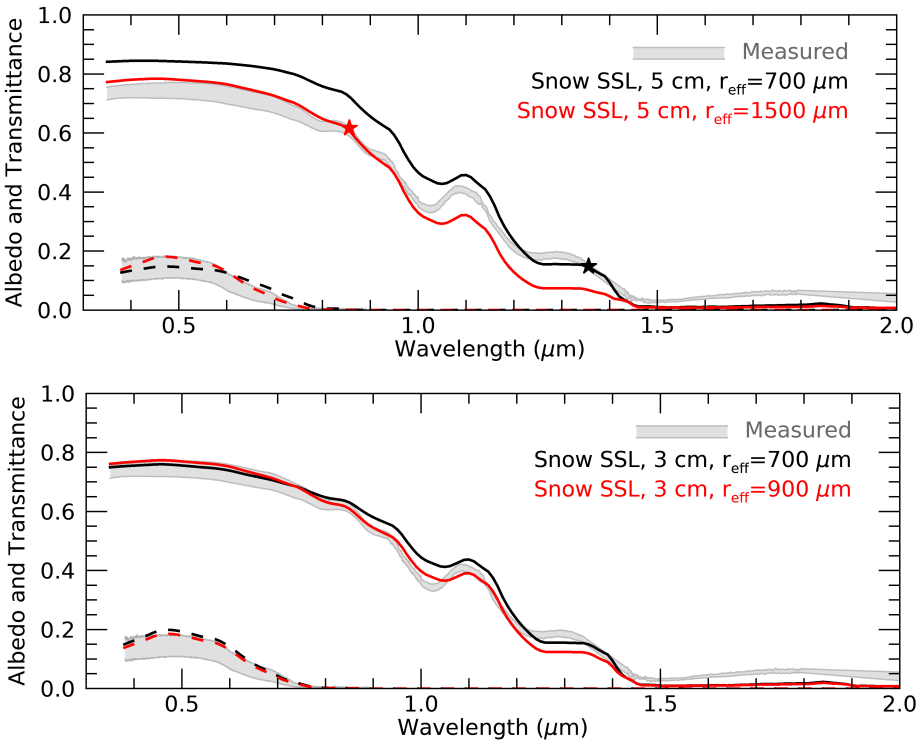


**Fig. 3.** Results of modeling method M3 (see Sec. 3.1), in which the SSL is represented as a snow layer, for the 3 July, 2010 case (top panel of Fig. 2). The solid lines are for albedo and dashed for transmittance. Upper panel: the SSL is substituted by a snow layer of equal physical thickness (5 cm) and consisting of spherical snow grains of density equal to that of the SSL, with an effective radius $r_{eff}$ = 700 µm (black) and $r_{eff}$ = 1500 µm (red). The stars indicate the wavelengths selected to infer the snow grain size. Bottom panel: same as the upper panel, but with snow properties (depth and density) different from those of the original SSL.

The simulations of sea ice albedo and transmittance shown in Figs. 2 and 3 tend to be at the high end of the observations in the visible spectrum, which indicates an underestimation of ice absorption. Black carbon is the main component of soot-like, absorbing impurities often found deposited on snow and ice [75]. Clarke and Noone [76] reported soot amounts mostly in the 5–50 nanograms of carbon per gram of snow (ng $g^{-1}$) range, corresponding to 0.005-0.05 ppm. Doherty et al. [77] measured BC concentrations around the Arctic (mostly in the top 50 cm of snow) ranging anywhere from 0.003 to 0.02 ppm, or occasionally even higher, from lower values near the North Pole to higher values at lower latitudes in the Arctic Ocean. The SHEBA observations show a lower average background BC of 0.0044 ppm for April snow [78]. Desired concentrations of BC can be included in any layer of the augmented COART model, with the IOPs given in the Optical Properties of Aerosols and Clouds (OPAC) software package [64]. The reduction in albedo caused by BC is a widely known effect [79,80]. Figure 4 contains the sensitivity of albedo and transmittance caused by increasing BC mass mixing ratios (0 ppm, 0.02 ppm, 0.04 ppm). These values were calculated to span the range of average BC concentrations indicated above, uniformly redistributed in the top 10 cm of ice in the model. As expected, contamination from

Optics EXPRESS

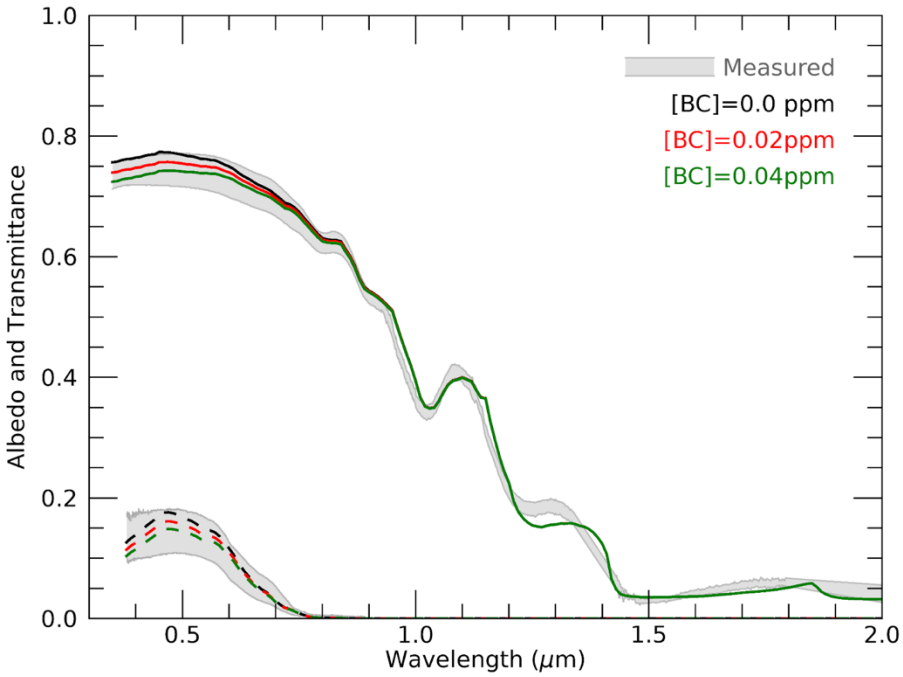


**Fig. 4.** Sensitivity to albedo (solid) and transmittance (dashed) to the addition of contamination from soot-like, BC particulate spanning amounts typical of the panarctic. The black lines are the spectra modeled with method M1 for 3 July, 2010 (top panel in Fig. 2).

such absorbing impurities (red and green curves) reduces the sea ice albedo and transmittance in the visible part of the spectrum, leading to an improvement in the model-observation comparison.

### *3.3. Bare, multi-year ice*

#### 3.3.1. Data

Data for MYI were measured during the SHEBA field experiment (also conducted in the Arctic Ocean) on 21 July, 1998. The total ice thickness measured *in situ* is 218 cm, and a few centimeters of surface granular layer was reported. The albedo and transmittance measurements [81,82] were collected with two different spectroradiometers: a Spectron Engineering SE-590 (for wavelengths in the 400-2000 nm range) and an Analytical Spectral Devices Ice-1 (400-800 nm). The SZA, calculated from time and location, is 60°.

A very limited number of cores were acquired during SHEBA [D. Perovich, *personal comm.*], which were not strictly co-located with the optical measurements. The salinity profiles (1 ppt and 3 ppt) were assumed for the DL and IL in the simulations, covering the mean salinity values reported for MYI, at least in the bulk of the ice [22,83]. As for FYI, the SSL is assumed desalinated. Since the SSL maintains a consistent microstructural profile throughout the melt season on all types of bare ices [27,69], we use the same measured depth and density of SSL as the FYI. Initial densities of 0.85 g/cm$^3$ and 0.91 g/cm$^3$ are applied to the DL and IL, respectively.

#### 3.3.2. Results

The difference between FYI and MYI mainly resides in the values of total thickness (generally higher for MYI), the salinity and the IL density (both generally lower). Typically, MYI has more cavities due to the flushing of melt water and is thicker than FYI; therefore, it has higher albedo and lower transmittance.

Optics EXPRESS

In Fig. 5, the gray lines correspond to the measurements collected with the two spectroradiometers. The red (blue) lines in the upper panel show the albedo and transmittance obtained using approach M1 when the salinity is 3 ppt (1 ppt). The results obtained using approach M2 are virtually identical (not shown). The inferred IL density is 0.915 g/cm$^3$ (0.910 g/cm$^3$) when the salinity is 3 ppt (1 ppt). The low-salinity case was included because MYI can be highly desalinated due to meltwater flushing [84]. In this case, a slight adjustment in IL density yields essentially the same results, indicating that the AOPs are less sensitive to salinity than to density. It should be noted that the transmittance through the MYI is very small (all transmittance curves are multiplied by a factor of ten for clarity), implying that the measurement uncertainty is significant. Nevertheless, fairly good agreement is found in both albedo and transmittance with both modeling approaches.

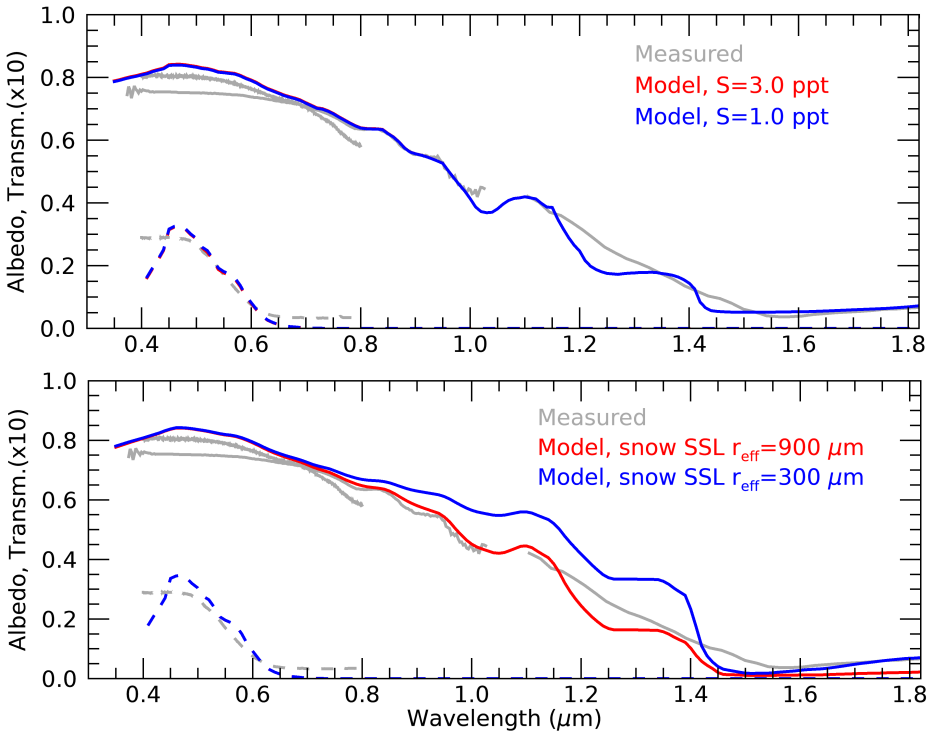


**Fig. 5.** Comparison of modeled sea ice albedo (colored solid lines) and transmittance (colored dashed lines) with SHEBA measurements of MYI (gray curves, from two different spectrometers as described in the text). For clarity, all the transmittance curves are multiplied by a factor of ten. Top panel: MYI on 21 July, 1998 (thickness 2.18 m), modeled with inferred bubble scattering (method M1). The red and blue represent two different salinities used in modeling. Lower panel: same as for the top panel, but with the ice SSL replaced by a snow layer (method M3).

As done for the FYI case, we also test the substitution of the SSL with a layer of snow (approach M3). For the same reason described for the FYI, good model-observation agreement cannot be achieved if the SSL is represented by a snow layer with the same physical properties (depth and density), and so in the lower panel we show the modeling results with a reduced snow depth of 3 cm and density 0.3 g/cm$^3$. With an inferred snow grain size $r_{eff}$ = 900 μm, the model-observation agreement is of similar quality as using an icy SSL for wavelengths <1.4 μm (red), but is consistently lower at longer wavelengths where the albedo is largely determined by

Optics EXPRESS

the grain size in the thin layer of snow. Our test shows that the grain size must be reduced to $r_{eff}$ <300 μm (blue) in order to fit the albedo at the longest wavelengths, but the observations at middle wavelengths are then drastically overestimated. Moreover, such small grain sizes are typically associated with pristine snow, not suitable to simulate the "granular" nature of the SSL. These simulations show that the modeling approaches M1 and M2 (3-layer ice model) offer superior performance compared to approach M3 that considers an SSL composed of snow.

The systematic overestimation of the observations in the visible region indicates insufficient in-ice absorption accounted for by the model. Several species can differentially affect the spectral radiation transport within the ice column, and observations have shown that ice-algae or chlorophyll pigments are often present [85–87]. Large seasonal variations of algal pigments (from 0.01 mg/m$^3$ in April to 0.5 mg/m$^3$ in June) were reported, with higher concentration at the bottom and top ice layers [88,89]. For the MYI case shown in the upper panel of Fig. 5, Fig. 6 shows that the simple assumption of a Chl-a concentration of 0.3 mg/m$^3$ uniformly distributed across the ice column would significantly lower the transmittance in the visible (green lines), therefore improving the model agreement. Nevertheless, the effect on albedo is much smaller and that in the near infrared is negligible. As done for FYI, we also tested the inclusion of BC particles in the SSL and DL (upper 18 cm, about the ice freeboard depth) with a concentration of 0.01 ppm (blue lines). Both the albedo and the transmittance in the visible spectrum are reduced and the model-observation agreement is improved.

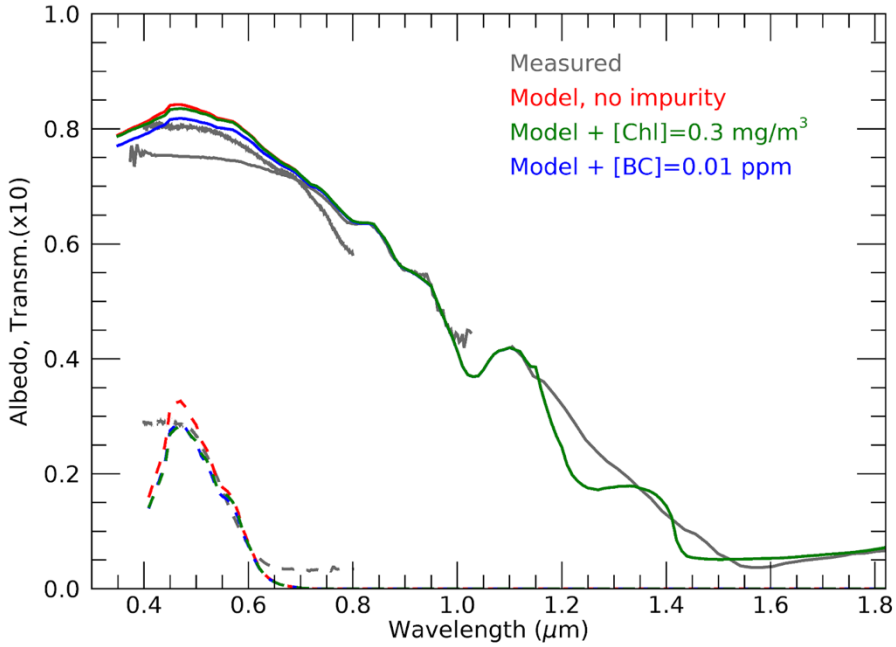


**Fig. 6.** Model sea ice albedo (solid colored lines) and transmittance (dashed colored lines) against SHEBA measurements of MYI (gray curves, from two different spectrometers as described in the text). Red: same as the red curve in the upper panel of Fig. 5. Green: same, but with ice algae included ([Chl-a] = 0.3 mg/m$^3$). Blue: same, but with 0.01 ppm of BC in the SSL and DL (18 cm) of ice. For clarity, all the transmittance curves are multiplied by a factor of 10.

Optics EXPRESS

### 3.4. Ponded ice

#### 3.4.1. Data

A series of ponded-ice observations, complete with measurements of pond depth and floor thickness, are available from ICESCAPE. The conditions ranged from completely overcast and a barely visible solar disk to clear skies.

The SSL is composed of coarse, crumbly grains of ice and voids of air. When meltwater appears at the top of the ice, its infiltration into the SSL is expected to significantly alter its physical and optical properties. Typically, a water-saturated SSL is indeed less reflective and more absorptive, or absent altogether (see L08). Indeed, percolation theory predicts the ice permeability to undergo a drastic transition when the brine volume exceeds ~5% [90,91], triggering the flushing of brine pockets through an increase in pore connectivity. Nevertheless, a thin top layer of so-called "superimposed" or "interposed" ice can still be possible in the presence of refrozen snowmelt. Such processes temporarily "seal" the ice surface, with appearance effects visible even to the unaided eye [70], and lead to top layer thicknesses of up to 10 cm.

We selected four cases with different total ice thickness (pond depth): 112 (8), 94 (11), 70 (20) and 70 (30) cm. There are two observations for the same pond on 3 July, 2010, showing only a slight difference in transmittance. Lacking observational information on pond water properties, the pond water is assumed to be pure freshwater with optical properties based on Pope and Fry [57] and Smith and Baker [58].

The salinity is also from observational data, and varies from about 0.5 ppt to 3.0 ppt [70]. Overcast conditions were reported for 2 July and 3 July (but with visible sun). As stated above, the presence and the exact properties of these clouds have a negligible effect on the AOPs, but for completeness a stratus cloud layer is modeled between altitudes of 0.5 km and 1.0 km with optical depth of 1.0.

The temperature at the water-ice interface at the bottom of the pond is set to 0°C, and that at the bottom of the ice to −2°C with a linear change through the ice column. Again, our tests show little effect for temperature variations in this narrow range.

#### 3.4.2. Results

We found that two ice layers (with a top layer thickness of 5 cm) are generally sufficient for the modeling. The densities of the upper and bottom layers are initially set at 0.85 and 0.91 g/cm$^3$, respectively, as for the DL and IL in the bare-ice cases. Because the spectral albedo of ponded ice in the near infrared is determined by the water and the transmittance is significantly larger than for bare ice, we use the measured transmittance at two wavelengths (0.5 and 0.7 μm) to scale the bubble scattering in the two ice layers as for the bare ice cases. The rows in Fig. 7 show the modeling results (red curves) for each of the four cases. The results of method M2 are not shown since they mostly overlap. The IL densities obtained with method M2 for the four cases are very similar: 0.9230, 0.9190, 0.9194 and 0.9193 g/cm$^3$ from top to bottom row.

It should be noted that albedo and transmittance were not measured exactly at the same location. Since the ice core thickness was reported for the transmittance measurements only, the safest assumption was to use the same thickness for the albedo simulations. This assumption limits the quality of the fit to the albedo, given the relatively small ice thicknesses for these ponded ice cases. However, the results show that using a simple 2-layer ice model the transmittance can be matched across all spectra, and the albedo agreement is satisfactory. The albedo between 0.8 and 1.4 μm, where the observations are systematically higher than the model, is dominated by the pond water properties and is not related to small uncertainties in the measurements of ice thickness. If the albedo measurements in the near-infrared are accurate (in this regime the energy at play and the subsequent instrumental S/N are very low), this fact indicates that some particle scattering might exist in the pond water, which is missing in the modeling. However, the model-observation discrepancy in albedo in the visible spectrum measured on 3 July, 2010, might

Optics EXPRESS

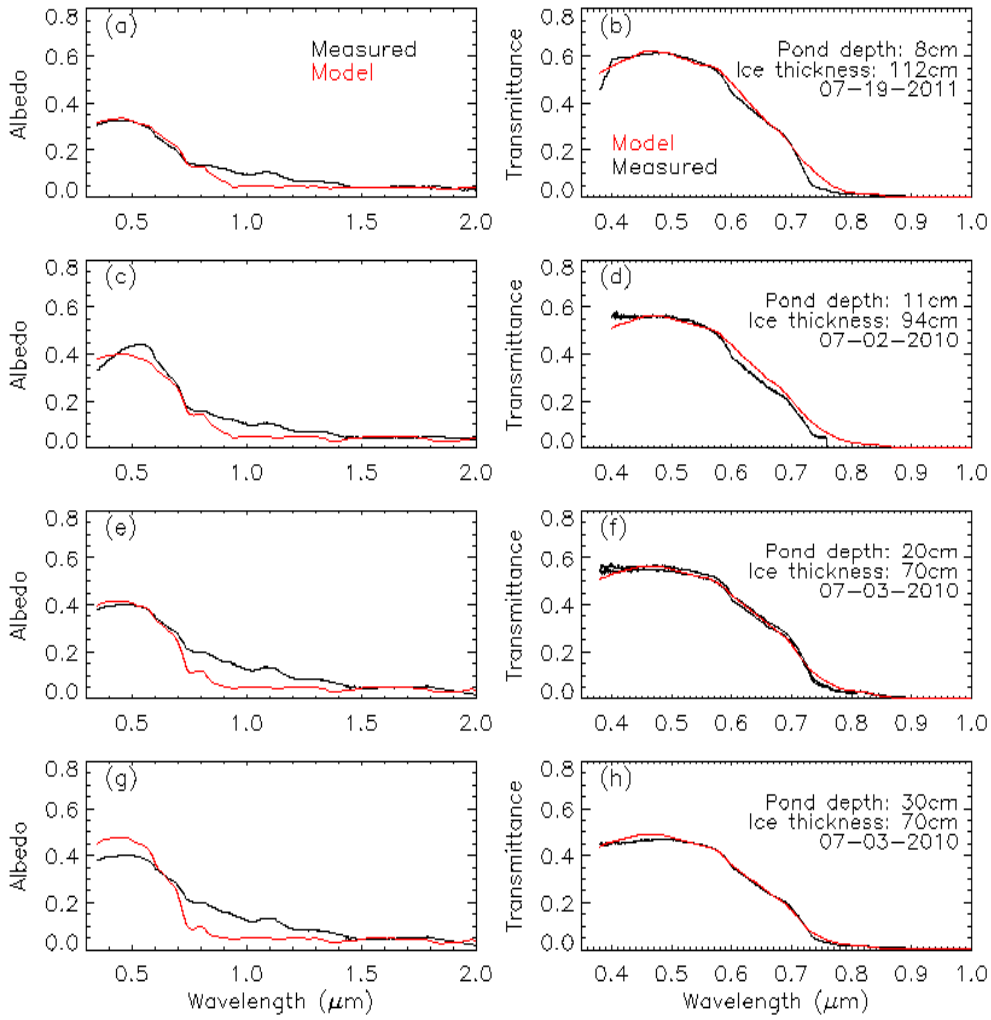


**Fig. 7.** Model albedo and transmittance (red curves) against ICESCAPE measurements (black curves) of ponded ice. The model is constrained using the measured pond depth (increasing from top to bottom), ice thickness and salinity. The ice underlying the melt ponds is divided into two layers.

still arise from inaccurate observational constraints on ice thickness and physical properties. Both the model and observation show that not only the pond water reduces the sea ice albedo, but also significantly impacts light transmission.

## 4. Conclusions

Radiative transfer in sea ice is deeply affected by the physical properties of the ice itself and the atmosphere above. A complete radiative transfer closure requires an exhaustive collection of co-located measurements of the ice column properties, which is often prohibitive considering the destructive nature of most core sampling techniques. To address this limitation, in this paper we introduced three different approaches to simulate *in situ* observations of the spectral albedo and transmittance of sea ice, using case studies where at least parts of the profiles (density, temperature, salinity) were available or could safely be assumed based on plausible ranges and

Optics EXPRESS

physical considerations. To this end, a fully-coupled radiative transfer model (COART) was extended to include a physically-based description of radiative processes within sea ice. The scattering properties of brine pockets and air bubbles, including the single scattering albedo and phase function, are calculated based on observed size distributions. The gas and brine volume are derived from the phase equations [59] as a function of ice density, salinity and temperature, i.e. the IOPs are parameterized directly as a function of its physical properties. Light-absorbing impurities can also be included in any layer of the ice. Contaminants such as BC and Chl-a are already included in the model, and the extension to any other inorganic particulate or taxonomic species whose absorption spectrum can be tabulated is trivial. To demonstrate the robustness and accuracy of COART in estimating the total absorption in the ice column, its performance is evaluated against albedo and transmittance observations of FYI, MYI, and ponded ice for the visible and near-infrared range of wavelengths. The model is highly sensitive to vertical variations in ice density or bubble scattering, and it is found that a minimum of three layers is required to adequately simulate the albedo and transmittance for bare FYI, in agreement with previous findings. This 3-layer structure can be morphologically associated with a granular, low-density surface scattering layer, a denser drained layer, and a high-density interior layer. The presence of the SSL in the radiative transfer calculation is fundamental to adequately model the observed albedo of bare ice in the near infrared.

The first two modeling approaches consider the SSL as an integral part of the ice column but with significantly lower density. Since bubble size distributions in the top ice layers have not been reported, in the first method we infer the scaling factors for the scattering coefficients needed to match the albedo in each ice layer. The scaling factor determined at selected wavelengths is then applied to the entire spectra. Physically, this scaling is equivalent to adjusting the bubble size distribution. The second method infers the ice density of the interior layer instead of the bubble scattering coefficient. Both methods consistently simulate the measured albedo and transmittance well and with nearly identical results, confirming appropriate physical treatment. The third modeling approach treats the SSL as a snow-like layer. The snow grain size is inferred based on albedo at a near infrared wavelength. This approach is similar to that presented in L15, but without the unphysical assumption of a spectrally-constant asymmetry factor. Moreover, L15 infer the scattering coefficients at each wavelength independently, while we determine scaling factors using spectrally-selective absorption features in each layer. It is found that satisfactory model-observation agreement cannot be obtained if the same depth and density of SSL are used for the substituted snow layer. Substantially different snow depth or density from the SSL have to be used in order to obtain reasonable agreement with measurements. In addition, the albedo at the longest wavelengths ($>1.4\,\mu$m) is generally underestimated in this approach, unless the snow grain size is reduced to less than about 300 µm, typical of new snow rather than of a granular layer. Conversely, modeling the SSL as an ice layer produces a higher albedo in the near infrared and thus better overall spectral agreement with the observations.

For ponded ice, a 2-layer ice model agrees closely with the measured AOPs for a range of pond depths. Depending on the pond depth, the albedo (transmittance) is significantly lower (higher) than that of bare ice, and transmittance decreases with pond depth for similar ice thicknesses below. The albedo is determined by the optical properties of the pond in the near infrared, and by those of the ice below in the visible. Discrepancies between model and observations in the near infrared (0.8–1.4 µm) suggests the existence of particle scattering in the pond water, which is not included in the model (although the albedo measurements are less accurate at these wavelengths). For all ice types, when pure ice and pure water are assumed, there appears to be insufficient absorption in the visible part of the spectrum. Contamination by either BC or Chl-a very effectively reduces both the albedo and the transmittance in the visible, providing an additional degree of freedom during fitting procedures to improve the agreement with the observations.

Optics EXPRESS

The fine-tuning of the AOPs of sea ice as a function of the descriptive physical parameters makes the augmented COART model a valuable tool to represent the complex radiative processes in the cryosphere. From a retrieval point of view, this forward code can be embedded within an inversion scheme to provide an optimal search for the chosen set of free parameters. An accurate and efficient radiative transfer model is also required for climate models, which use simple AOP parameterizations for sea ice. The integration of a suitable form of this engine into the state-of-the-art NASA GISS ModelE [92] is ongoing, in order to provide accurate estimates of the fluxes reflected back to the atmosphere and transmitted into the ocean, as well as the radiative absorption within the ice medium that determines the evolution of its thickness. Due to the complex inter-relationships among ice physical properties, IOPs and AOPs, if the IOP parameterization is physically incorrect it is unlikely to produce simultaneous fits to albedo, transmittance, and absorption across all wavelengths with the described modeling approaches. Should accurate density profiles be available, the relationships between the IOPs and the ice properties can be refined by improving, for example, the parameterizations of the size distribution of air bubbles and brine inclusions. For these reasons, this and related works advocate the deployment of comprehensive measurement suites capable of adequate data quality, especially regarding the vertical profiles of density, temperature, and salinity which are notoriously challenging. A better characterization of impurities, such as soot-like, dust-like and algal particulates is also desirable, since these contaminants are often present in the ice column as well as in melt pond waters.

## 5. Appendix

A complete report on the sensitivity of albedo and transmittance to the variables in the augmented COART model is prohibitive for the main body of the paper. For this reason, we collect in this Appendix some results that justify some of the claims made in the paper. First, we justify the statements on the need of using at least three layers when modeling bare ice. The black curves in Fig. 8 show that reasonable fits can be obtained for the two analyzed bare-ice cases, when three layers are used each defined by an independent value of density (see the values listed with the "3L" item in the legend). Although this partitioning reflects the most detailed description available for the morphology of bare ice (an SSL, a DL and an IL), the SSL thickness here is 1 cm (decreasing layer thickness is equivalent to scaling down the scattering coefficient). It was found impossible to obtain good agreement both at visible and infrared wavelengths for thicker SSLs, as observed and used in approach M1 (see main text). The reason is that the curves in Fig. 8 assume the same air bubble distribution (which determines the density) across all layers. This is a gross approximation, as available bubble size distributions are based on measurements collected exclusively for the interior of the ice, while the SSL (and the DL) are expected to exhibit significantly different distributions. Very recent thickness and density measurements of SSL samples collected at different times and locations for FYI have revealed remarkable consistency [69]. Based on these observations, in approach M1 the SSL thickness was constrained to 5 cm and the SSL density (which exhibits a consistent gradient to be resolved by an arbitrary number of sublayers) was modeled using two sublayers. A scaling factor was then applied to the scattering coefficient in these two layers, which accommodates the expected variation in the size distribution with respect to the IL. This approach yielded very good agreement with the observations.

Regardless of SSL thickness and bubble size distributions, Fig. 8 clearly shows that if any combination of the densities used for the 3 L model is further employed to reduce the number of layers the quality of the fits is degraded to an unacceptable degree. A single layer is insufficient to adequately reproduce both the albedo and transmittance, as shown by the blue lines that are far off the measured ranges of both quantities. The 2-layer model (red and orange curves) also incurs in the same problem. Specifically, it is not possible to fit to a satisfactory degree the albedo at visible and infrared wavelengths simultaneously, and the modeled transmittance is still off the observed range.

Optics EXPRESS

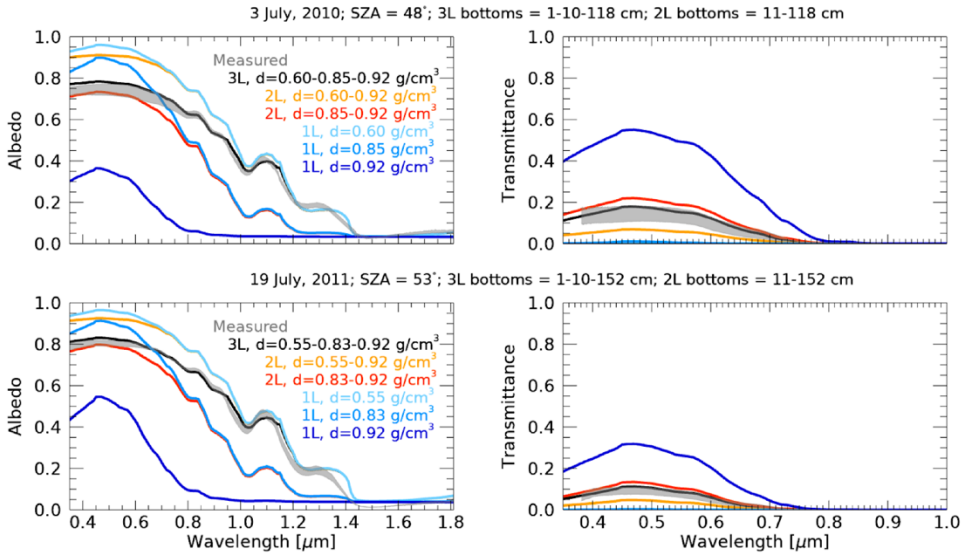


**Fig. 8.** Sensitivity of modeled albedo and transmittance to the number of layers employed in the simulations. The gray areas correspond to the range of measurements collected during the ICESCAPE FYI observations presented in the main body of the paper (Fig. 2): the top panels are for 3 July, 2010, and the bottom panels for 19 July, 2011. An ice model consisting of three layers (black, with the densities of the SSL, DL and IL given under the "3L" item in the legend) is needed to obtain an adequate fit. The results for 1-layer ("1L", shades of blue) and 2-layer ("2L", red and orange) models with different combinations of the densities used in the 3-layer model are added for comparison. The transmittance curves for the two lowest densities in the 1 L model are essentially zero. The salinity profiles are from the *in-situ* measurements as used in the approaches explained in the main text. Averages (weighted by each layer thickness) are used for the 2 L and 1 L models.

In the figures that follow, we take as reference the 3-layer model used in Fig. 8 for the July 03, 2010 case. Figure 9 illustrates the small sensitivity of the albedo to SZA (increasing for increasing SZA) in the visible, but measurable differences appear as the wavelength increases. The sensitivity of the transmittance is negligible. It should be noted that a clear sky is assumed here. If atmospheric clouds and aerosols are introduced, the sensitivity will be smaller (see Fig. 12).

In Fig. 10 we focus on the sensitivity to temperature at the top of the ice. Again, the reference curve (black) is for the case on 3 July, 2010, but here the temperature is set as uniform at −2°C throughout the ice column. The red and blue curves correspond instead to temperatures at the top of the ice of −10°C and −20°C. The temperature at the bottom is kept at −2°C, a value that very closely approximates that commonly observed at the ice/ocean interface. The temperature in each layer is the result of linear interpolation between top and bottom temperatures. The sensitivity is minimal. While using a top temperature of −10°C would slightly improve the fit to the albedo data in the visible for the cases presented in Fig. 8, the effect on transmittance is opposite. Considering the low sensitivity, in the paper we have therefore adopted a temperature of T=-2°C at the top of the ice, which also well applies to summer conditions.

Figure 11 shows the optical effect of different salinity profiles. The maximum value (10 ppt) is a rare occurrence anywhere in the ice column, but was deemed a good maximum value in order to capture the full range of potential variability. Detectable changes are present up to the NIR, and are significant in the visible. In most situations, it is observed that the model predicts

Optics EXPRESS

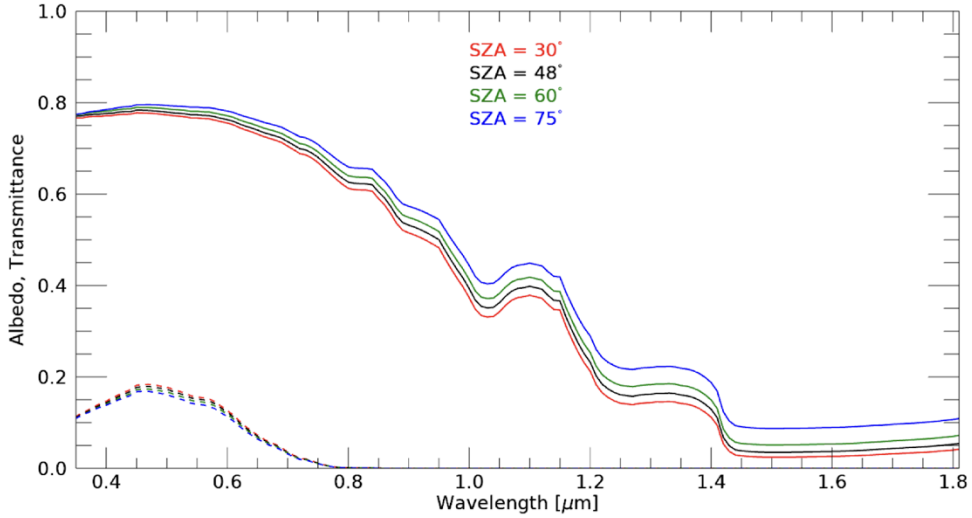


**Fig. 9.** Sensitivity of the model curves in Fig. 2 (black, corresponding to the July 3, 2010, case) to the Solar Zenith Angle (SZA = 30°, 48°, 60°, 75°). Solid lines are for albedo and dashed lines are for transmittance.

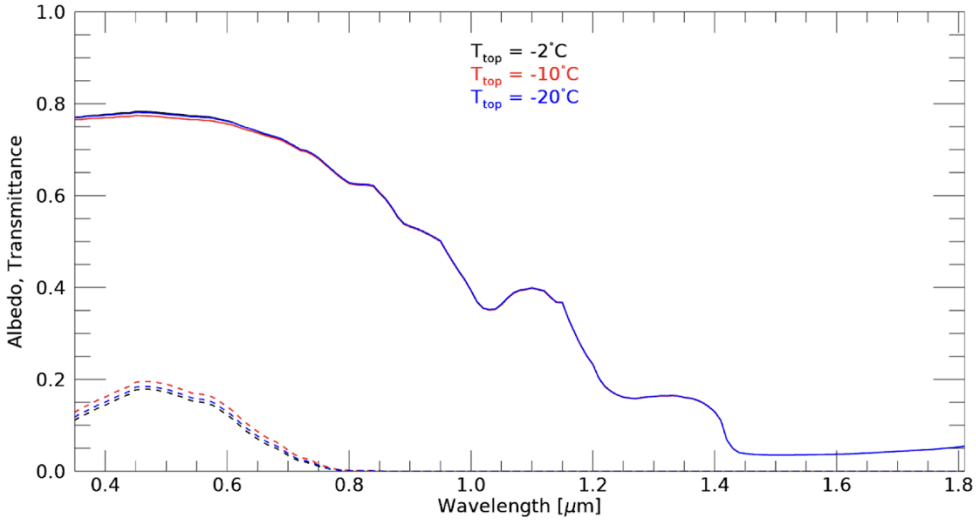


**Fig. 10.** As in Fig. 9, but for a SZA = 48° and temperature variations at the top of the ice (T = -2°C, -10°C, −20°C).

Optics EXPRESS

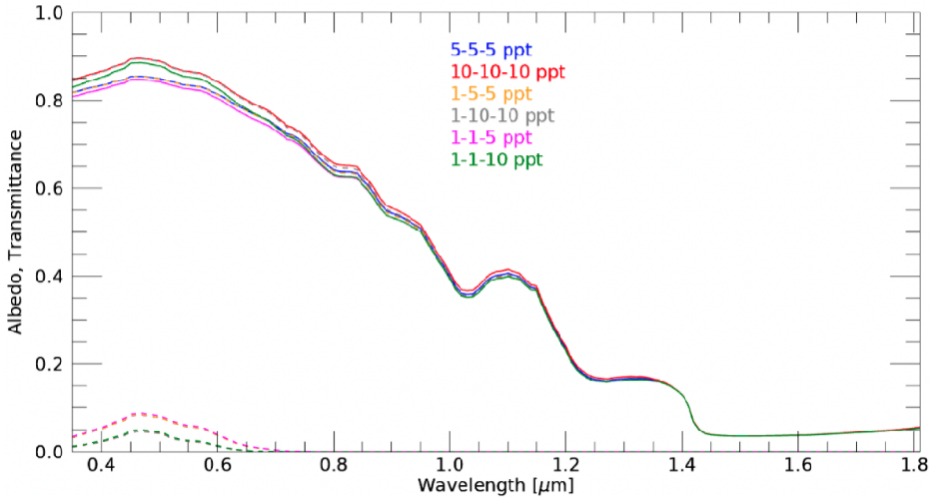


**Fig. 11.** Sensitivity of the black model curves in Fig. 1 (corresponding to the July 3, 2010, case) to different salinity profiles in the three layers.

maximum differences in both albedo and transmittance of up to 0.05 in correspondence of their peaks in the visible.

Another factor worth considering, and that deals with the illumination conditions, is the presence of cloud cover. Low-level stratus clouds are very common in the Arctic summer [36]. In Fig. 12 we consider the presence of a cloud layer between 0.5 and 1 km in altitude, and of variable optical depths ($\tau$=0, 1, 10). The cloud properties are calculated for droplets of effective radius equal to 10 μm [93]. While the simulated spectral transmittance does not vary much (expected for ice as thick as this case, 118 cm), the sensitivity of the albedo to the different contributions of the direct and diffuse radiances to cloud optical depth is less than trivial. When a cloud is present ($\tau$>0), the sensitivity to the SZA is reduced. Appreciable differences are noted either for very low or very high SZAs, while for ~40°<SZA<~60° the albedo is essentially unaffected. The explanation of this fact resides in the Fresnel nature of the surface reflectivity. While the reflectivity for the diffuse component is insensitive to SZA and cloud optical depth, the specular reflectivity for the direct beam is rather low (and constant) for small angles of incidence (in this case, the SZA). It then decreases further around the Brewster angle, before exhibiting an almost exponential increase at grazing incidences, up to the 100% ideal limit of horizontal illumination. For increasing cloud optical depths, this non-monotonic dependence of the Fresnel reflectance on the SZA causes the albedo to increase if SZA<~40°, remain unaltered in the Brewster region (~40°<SZA<~60°), and decrease if SZA>~60°. For the observation on 3 July, 2010, the SZA was 48°, eliminating the need to consider a cloud layer in the model.

We conclude with some arguments on the ice roughness. Ice surfaces are naturally rough, and the extended COART model offers full flexibility in the treatment of roughness [50]. A Gaussian equation is used to describe the statistical distribution of the surface facets, in a similar fashion as the Cox-Munk model used to parameterize the distribution of ocean waves [56]. The extension to any other distribution is trivial, should observational evidence indicate the need. Since no sunglint has been reported on ice surfaces and granular features are observed, the sea ice surface is likely rougher than a calm ocean surface. Lacking appropriate measurements of surface roughness statistics, we simply used σ=0.5 and σ=0.1 for the ice and pond surface, respectively. Based on the Cox-Munk formulation, σ=0.1 represents a minimal ocean surface roughness (wind speed = 1.4 m/s). For the ice cases in this study, a coarsely-grained surface layer was observed.

Optics EXPRESS

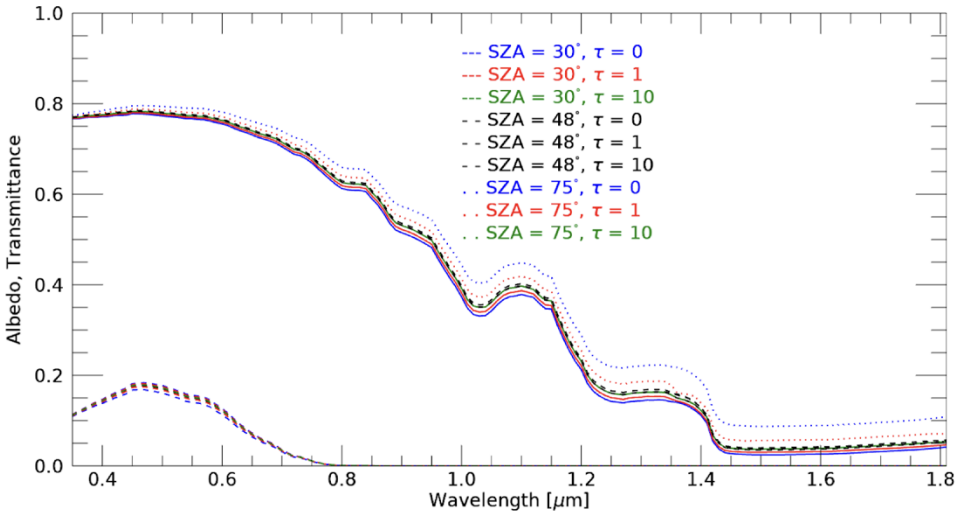


**Fig. 12.** Sensitivity of the albedo (solid) and transmittance (dashed) to cloud cover of variable optical depth ($\boldsymbol{\tau}$=0, 1, 10), and for different SZAs. The three curves for SZA = 48° essentially overlap and are all shown with black dashed lines, even for the albedo. Note the opposite effect of increasing cloud optical depth on the albedo for low and high SZAs, here set to SZA = 20° (solid lines) and SZA = 75° (dotted lines).

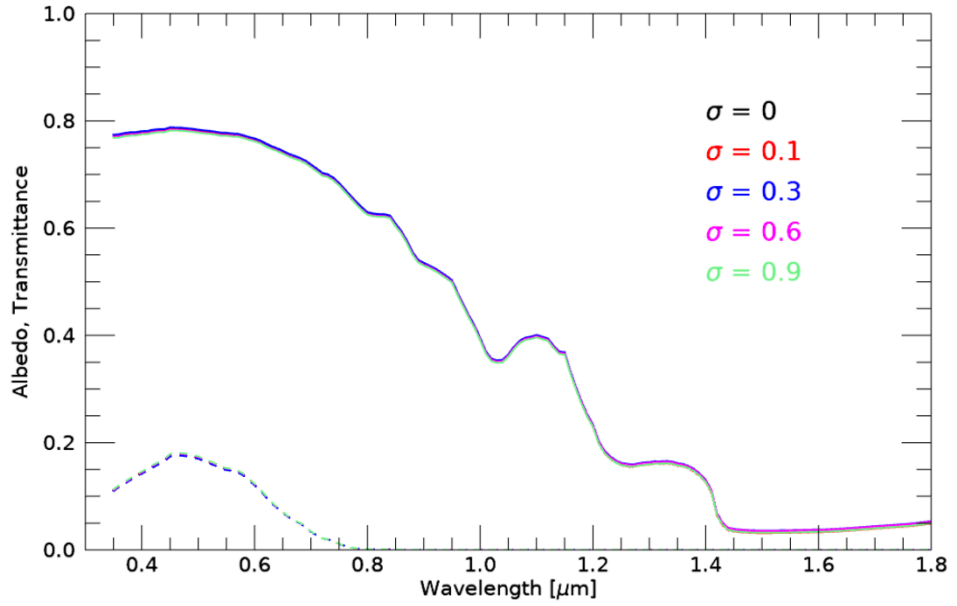


**Fig. 13.** Sensitivity of the albedo (solid lines) and transmittance (dashed lines) to the value, σ, chosen to model the variance of the distribution of ice surface slopes (ice roughness). The variations in albedo and transmittance are negligible.

Optics EXPRESS

Because the SSL appears granular, many surface facets must have large tilt angles. A value of σ=0.5 implies that 95% (99.7%) of the facet normals are <45° (<56°) from the local vertical. No observational data exist to constrain the roughness value, but again (differently from its impact on the radiance) the effect on the irradiance is small. While surface roughness affects both the direct and diffuse light components (and therefore the surface bidirectional reflectance distribution function as shown in [44]), its effect on albedo and transmittance is small, as demonstrated in Fig. 13.

**Funding.** National Aeronautics and Space Administration ROSES IDS (Interdisciplinary Research in Earth Science) (80NSSC20K1523).

**Acknowledgments.** We are grateful to Dr. Bonnie Light for continuous assistance with the interpretation of the ICESCAPE and SHEBA datasets, and to Dr. Melinda Webster and Dr. Maddie Smith for very informative discussions on the nature of the SSL.

**Disclosures.** The authors declare that they have no conflict of interest.

**Data availability.** The data from the ICESCAPE campaign were obtained from the SeaWiFS Bio-optical Archive and Storage System (SeaBASS) portal, see Ref. [73]. The data from the SHEBA campaign were downloaded from the dedicated UCAR portal. More specifically, spectral albedo measurements were retrieved from Ref. [81] and transmittance data from Ref. [82]. Data underlying the results presented in this paper are not publicly available at this time but may be obtained from the authors upon reasonable request.

## References

1. F. Fetterer, K. Knowles, W. Meier, M. Savoie, and A. K. Windnagel, "Sea Ice Index, Version 3," National Snow and Ice Data Center (2017).
2. M. C. Serreze and R. G. Barry, "Processes and impacts of Arctic amplification: A research synthesis," Global and Planetary Change **77**(1-2), 85–96 (2011).
3. R. Kwok and N. Untersteiner, "The thinning of Arctic sea ice," Phys. Today **64**(4), 36–41 (2011).
4. J. C. Stroeve, V. Kattsov, A. Barrett, M. Serreze, T. Pavlova, M. Holland, and W. N. Meier, "Trends in Arctic sea ice extent from CMIP5, CMIP3 and observations," Geophys. Res. Lett. **39**(16), 1 (2012).
5. J. A. Curry, J. L. Schramm, and E. E. Ebert, "Sea Ice-Albedo Climate Feedback Mechanism," J. Clim. **8**(2), 240–247 (1995).
6. A. Hall, "The Role of Surface Albedo Feedback in Climate," J. Clim. **17**(7), 1550–1568 (2004).
7. S. J. Déry and R. D. Brown, "Recent Northern Hemisphere snow cover extent trends and implications for the snow-albedo feedback," Geophys. Res. Lett. **34**(22), L22504 (2007).
8. S. Arndt and M. Nicolaus, "Retrieval of aerosol properties over the ocean from multispectral single-viewing-angle measurements of intensity and polarization: Retrieval approach, information content, and sensitivity study"Seasonal cycle and long-term trend of solar energy fluxes through Arctic sea ice," The Cryosphere **8**(6), 2219–2233 (2014).
9. P. C. Taylor, M. Cai, A. Hu, J. Meehl, W. Washington, and G. J. Zhang, "A decomposition of feedback contributions to polar warming amplification," J. Clim. **26**(18), 7023–7043 (2013).
10. F. Pithan and T. Mauritsen, "Arctic amplification dominated by temperature feedbacks in contemporary climate models," Nat. Geosci. **7**(3), 181–184 (2014).
11. A. Keen, E. Blockley, D. A. Bailey, J. Boldingh Debernard, M. Bushuk, S. Delhaye, D. Docquier, D. Feltham, F. Massonnet, and S. O'Farrell, "An inter-comparison of the mass budget of the Arctic sea ice in CMIP6 models," The Cryosphere **15**(2), 951–982 (2021).
12. D. Notz, A. Jahn, M. Holland, E. Hunke, F. Massonnet, J. Stroeve, B. Tremblay, and M. Vancoppenolle, "The CMIP6 Sea-Ice Model Intercomparison Project (SIMIP): understanding sea ice through climate-model simulations," Geosci. Model Dev. **9**(9), 3427–3446 (2016).
13. T. Koenigk, A. Devasthale, and K.-G. Karlsson, "Summer Arctic sea ice albedo in CMIP5 models," Atmos. Chem. Phys. **14**(4), 1987–1998 (2014).
14. S. Solomon, D. Qin, M. Manning, K. Averyt, and M. Marquis, *Climate Change 2007-the Physical Science Basis: Working Group I Contribution to the Fourth Assessment Report of the IPCC* (Cambridge university press, 2007), **4**.
15. T. C. Grenfell and G. A. Maykut, "The optical properties of ice and snow in the Arctic Basin," J. Glaciol. **18**(80), 445–463 (1977).
16. W. F. Weeks and S. F. Ackley, *The Growth, Structure, and Properties of Sea Ice* (Springer, 1986).
17. E. Hunke, D. Notz, A. Turner, and M. Vancoppenolle, "The multiphase physics of sea ice: a review for model developers," The Cryosphere **5**(4), 989–1009 (2011).
18. S. G. Warren, "Optical properties of ice and snow," Phil. Trans. R. Soc. A **377**(2146), 20180161 (2019).
19. S. F. Daly, *Frazil Ice Dynamics* (COLD REGIONS RESEARCH AND ENGINEERING LAB HANOVER NH, 1984).
20. I. A. Dmitrenko, C. Wegner, H. Kassens, S. A. Kirillov, T. Krumpen, G. Heinemann, A. Helbig, D. Schröder, J. A. Hölemann, and T. Klagge, "Observations of supercooling and frazil ice formation in the Laptev Sea coastal polynya," J. Geophys. Res. Oceans **115**(C5), C05015 (2010).

Optics EXPRESS


21. D. Notz and M. G. Worster, "In situ measurements of the evolution of young sea ice," J. Geophys. Res. Oceans **113**(C3), C03001 (2008).
22. H. Eicken, M. Lensu, M. Leppäranta, W. Tucker III, A. Gow, and O. Salmela, "Thickness, structure, and properties of level summer multiyear ice in the Eurasian sector of the Arctic Ocean," J. Geophys. Res. Oceans **100**(C11), 22697–22710 (1995).
23. M. Nicolaus, C. Katlein, J. Maslanik, and S. Hendricks, "Changes in Arctic sea ice result in increasing light transmittance and absorption," Geophys. Res. Lett. **39**(24), 2012GL053738 (2012).
24. W. B. Tucker III, A. J. Gow, and W. F. Weeks, "Physical properties of summer sea ice in the Fram Strait," J. Geophys. Res. Oceans **92**(C7), 6787–6803 (1987).
25. G. Timco and R. Frederking, "A review of sea ice density," Cold Reg. Sci. Technol. **24**(1), 1–6 (1996).
26. C. Polashenski, D. Perovich, and Z. Courville, "The mechanisms of sea ice melt pond formation and evolution," J. Geophys. Res. Oceans **117**(C1), 1 (2012).
27. B. Light, M. M. Smith, D. K. Perovich, M. A. Webster, M. M. Holland, F. Linhardt, I. A. Raphael, D. Clemens-Sewall, A. R. Macfarlane, P. Anhaus, and D. A. Bailey, "Arctic sea ice albedo: Spectral composition, spatial heterogeneity, and temporal evolution observed during the MOSAiC drift," Elementa: Sci. Anthropocene **10**(1), 000103 (2022).
28. B. Light, T. C. Grenfell, and D. K. Perovich, "Transmission and absorption of solar radiation by Arctic sea ice during the melt season," J. Geophys. Res. Oceans **113**(C3), C03023 (2008).
29. B. Light, D. K. Perovich, M. A. Webster, C. Polashenski, and R. Dadic, "Optical properties of melting first-year Arctic sea ice," J. Geophys. Res. Oceans **120**(11), 7657–7675 (2015).
30. T. C. Grenfell and D. K. Perovich, "Spectral albedos of sea ice and incident solar irradiance in the southern Beaufort Sea," J. Geophys. Res. Oceans **89**(C3), 3573–3580 (1984).
31. D. K. Perovich, T. C. Grenfell, B. Light, and P. V. Hobbs, "Seasonal evolution of the albedo of multiyear Arctic sea ice," J. Geophys. Res. Oceans **107**(C10), 8044 (2002).
32. J. Ehn, M. Granskog, T. Papakyriakou, R. Galley, and D. Barber, "Surface albedo observations of Hudson Bay (Canada) landfast sea ice during the spring melt," Ann. Glaciol. **44**, 23–29 (2006).
33. N. Untersteiner, A. Thorndike, D. Rothrock, and K. Hunkins, "AIDJEX revisited: A look back at the US-Canadian Arctic ice dynamics joint experiment 1970-78," Arctic **60**(3), 327–336 (2007).
34. M. Nicolaus, S. Gerland, S. R. Hudson, S. Hanson, J. Haapala, and D. K. Perovich, "Seasonality of spectral albedo and transmittance as observed in the Arctic Transpolar Drift in 2007," J. Geophys. Res. Oceans **115**(C11), C11011 (2010).
35. T. Taskjelle, S. R. Hudson, M. A. Granskog, M. Nicolaus, R. Lei, S. Gerland, J. J. Stamnes, and B. Hamre, "Spectral albedo and transmittance of thin young Arctic sea ice," J. Geophys. Res. Oceans **121**(1), 540–553 (2016).
36. J. Curry, P. Hobbs, M. King, D. Randall, P. Minnis, G. Isaac, J. Pinto, T. Uttal, A. Bucholtz, and D. Cripe, "FIRE Arctic clouds experiment," Bull. Am. Meteorol. Soc. **81**(1), 5–29 (2000).
37. M. Nicolaus, D. K. Perovich, G. Spreen, M. A. Granskog, L. von Albedyll, M. Angelopoulos, P. Anhaus, S. Arndt, H. J. Belter, and V. Bessonov, "Overview of the MOSAiC expedition: Snow and sea ice," Elem. Sci. Anth. **10**(1), 000046 (2022).
38. P. Schmidt, S. Taylor, P. Boisvert-McPartland, L. Bucholtz, A. Cesana, G. DeMott, P. Fridland, A. Kahn, R. Kurtz, N. McFarquhar, G. Moore, R. Parker, C. Redemann, J. Segal-Rozenhaimer, M. Soloman, A. Tilling, R. Zamora, and L. Zuidema, "Arctic Radiation-Cloud-Aerosol-Surface Interaction Experiment (ARCSIX)," (n.d.).
39. T. C. Grenfell, "A radiative transfer model for sea ice with vertical structure variations," J. Geophys. Res. **96**(C9), 16991 (1991).
40. P. Briegleb and B. Light, *A Delta-Eddington Mutiple Scattering Parameterization for Solar Radiation in the Sea Ice Component of the Community Climate System Model* ((No. NCAR/TN-472 + STR). University Corporation for Atmospheric Research, 2007).
41. Z. Jin and K. Stamnes, "Radiative transfer in nonuniformly refracting layered media: atmosphere-ocean system," Appl. Opt. **33**(3), 431–442 (1994).
42. B. Hamre, J.-G. Winther, S. Gerland, J. J. Stamnes, and K. Stamnes, "Modeled and measured optical transmittance of snow-covered first-year sea ice in Kongsfjorden, Svalbard," J. Geophys. Res. Oceans **109**(C10), C10006 (2004).
43. B. Hamre, S. Stamnes, K. Stamnes, and J. Stamnes, "AccuRT: A versatile tool for radiative transfer simulations in the coupled atmosphere-ocean system," in *AIP Conference Proceedings* (Author(s), 2017).
44. M. L. Lamare, J. D. Hedley, and M. D. King, "The effects of surface roughness on the calculated, spectral, conical-conical reflectance factor as an alternative to the bidirectional reflectance distribution function of bare sea ice," The Cryosphere **17**(2), 737–751 (2023).
45. B. Light, G. Maykut, and T. Grenfell, "A temperature-dependent, structural-optical model of first-year sea ice," J. Geophys. Res. Oceans **109**(C6), C06013 (2004).
46. D. Flocco, D. L. Feltham, and A. K. Turner, "Incorporation of a physically based melt pond scheme into the sea ice component of a climate model," J. Geophys. Res. Oceans **115**(C8), C08012 (2010).
47. A. Röosel, L. Kaleschke, and G. Birnbaum, "Melt ponds on Arctic sea ice determined from MODIS satellite data using an artificial neural network," The Cryosphere **6**(2), 431–446 (2012).
48. H. Niehaus, G. Spreen, G. Birnbaum, L. Istomina, E. Jäkel, F. Linhardt, N. Neckel, N. Fuchs, M. Nicolaus, and T. Sperzel, "Sea Ice Melt Pond Fraction Derived From Sentinel-2 Data: Along the MOSAiC Drift and Arctic-Wide," Geophys. Res. Lett. **50**(5), e2022GL102102 (2023).

Optics EXPRESS


49. E. Zege, A. Malinka, I. Katsev, A. Prikhach, G. Heygster, L. Istomina, G. Birnbaum, and P. Schwarz, "Algorithm to retrieve the melt pond fraction and the spectral albedo of Arctic summer ice from satellite optical data," Remote Sens. Environ. **163**, 153–164 (2015).
50. Z. Jin, T. P. Charlock, K. Rutledge, K. Stamnes, and Y. Wang, "Analytical solution of radiative transfer in the coupled atmosphere-ocean system with a rough surface," Appl. Opt. **45**(28), 7443–7455 (2006).
51. Z. Jin, T. P. Charlock, and K. Rutledge, "Analysis of broadband solar radiation and albedo over the ocean surface at COVE," J. Atmos. Oceanic Technol. **19**(10), 1585–1601 (2002).
52. Z. Jin, T. P. Charlock, K. Rutledge, G. Cota, R. Kahn, J. Redemann, T. Zhang, D. A. Rutan, and F. Rose, "Radiative transfer modeling for the CLAMS experiment," J. Atmos. Sci. **62**(4), 1053–1071 (2005).
53. K. Stamnes, S.-C. Tsay, W. Wiscombe, and K. Jayaweera, "Numerically stable algorithm for discrete-ordinate-method radiative transfer in multiple scattering and emitting layered media," Appl. Opt. **27**(12), 2502 (1988).
54. A. Berk, G. Anderson, P. Acharya, and E. Shettle, "MODTRAN5. 2.0. 0 User's Manual; Spectral Science Inc," Burlingt, MA, USA (2008).
55. S. G. Warren and R. E. Brandt, "Optical constants of ice from the ultraviolet to the microwave: A revised compilation," J. Geophys. Res. **113**(D14), D14220 (2008).
56. C. Cox and W. Munk, "Measurement of the Roughness of the Sea Surface from Photographs of the Sun's Glitter," J. Opt. Soc. Am. **44**(11), 838–850 (1954).
57. R. M. Pope and E. S. Fry, "Absorption spectrum (380–700 nm) of pure water. II. Integrating cavity measurements," Appl. Opt. **36**(33), 8710–8723 (1997).
58. R. Smith and K. Baker, "Optical properties of the clearest natural waters," Appl. Opt. **20**(2), 177–184 (1981).
59. G. F. Cox and W. F. Weeks, "Equations for determining the gas and brine volumes in sea-ice samples," J. Glaciol. **29**(102), 306–316 (1983).
60. B. Light, G. A. Maykut, and T. C. Grenfell, "Effects of temperature on the microstructure of first-year Arctic sea ice," J. Geophys. Res. Oceans **108**(C2), 1 (2003).
61. T. C. Grenfell, "A theoretical model of the optical properties of sea ice in the visible and near infrared," J. Geophys. Res. Oceans **88**(C14), 9723–9735 (1983).
62. W. J. Wiscombe, "Improved Mie scattering algorithms," Appl. Opt. **19**(9), 1505–1509 (1980).
63. D. K. Perovich and A. J. Gow, "A quantitative description of sea ice inclusions," J. Geophys. Res. Oceans **101**(C8), 18327–18343 (1996).
64. M. Hess, P. Koepke, and I. Schult, "Optical properties of aerosols and clouds: The software package OPAC," Bull. Am. Meteorol. Soc. **79**(5), 831–844 (1998).
65. R. McClatchey, "Optical Properties of the Atmosphere," Report AFCRL-72-0497, Environmental Research Papers **411**, (1972).
66. H. R. Gordon and A. Y. Morel, "Remote Assessment of Ocean Color for Interpretation of Satellite Visible Imagery," Lecture Notes on Coastal and Estuarine Studies (1983).
67. A. Morel and S. Maritorena, "Bio-optical properties of oceanic waters- A reappraisal," J. Geophys. Res. **106**(C4), 7163–7180 (2001).
68. A. Morel and B. Gentili, "Radiation transport within oceanic (case 1) water," J. Geophys. Res. Oceans **109**(C6), C06008 (2004).
69. A. R. Macfarlane, R. Dadic, M. M. Smith, B. Light, M. Nicolaus, H. Henna-Reetta, M. Webster, F. Linhardt, S. Hämmerle, and M. Schneebeli, "Evolution of the microstructure and reflectance of the surface scattering layer on melting level Arctic sea ice," Elementa Science of the Anthropocene In Press (2023).
70. C. Polashenski, D. K. Perovich, K. E. Frey, L. W. Cooper, C. I. Logvinova, R. Dadic, B. Light, H. P. Kelly, L. D. Trusel, and M. Webster, "Physical and morphological properties of sea ice in the Chukchi and Beaufort Seas during the 2010 and 2011 NASA ICESCAPE missions," Deep Sea Res., Part II **118**, 7–17 (2015).
71. Z. Jin, T. P. Charlock, P. Yang, Y. Xie, and W. Miller, "Snow optical properties for different particle shapes with application to snow grain size retrieval and MODIS/CERES radiance comparison over Antarctica," Remote Sens. Environ. **112**(9), 3563–3581 (2008).
72. W. J. Wiscombe and S. G. Warren, "A model for the spectral albedo of snow. I: Pure snow," J. Atmos. Sci. **37**(12), 2712–2733 (1980).
73. D. Perovich, "ICESCAPE 2010 and ICESCAPE 2011, NASA Ocean Biology DAAC (SeaBASS)", DOI: 10.5067/SEABASS/ICESCAPE/DATA001 (2011).
74. E. Salganik, C. Katlein, B. A. Lange, I. Matero, R. Lei, A. A. Fong, S. W. Fons, D. Divine, M. Oggier, and G. Castellani, "Temporal evolution of under-ice meltwater layers and false bottoms and their impact on summer Arctic sea ice mass balance," Under Review (2023).
75. A. Marks and M. King, "The effects of additional black carbon on the albedo of Arctic sea ice: variation with sea ice type and snow cover," The Cryosphere **7**(4), 1193–1204 (2013).
76. A. Clarke and K. Noone, "Soot in the Arctic snowpack: a cause for perturbations in radiative transfer," Atmos. Environ. **19**(12), 2045–2053 (1985).
77. S. Doherty, S. Warren, T. Grenfell, A. Clarke, and R. Brandt, "Light-absorbing impurities in Arctic snow," Atmos. Chem. Phys. **10**(23), 11647–11680 (2010).
78. T. C. Grenfell, B. Light, and M. Sturm, "Spatial distribution and radiative effects of soot in the snow and sea ice during the SHEBA experiment," J. Geophys. Res. Oceans **107**(C10), 8032 (2002).

Optics EXPRESS


79. S. G. Warren and W. J. Wiscombe, "A model for the spectral albedo of snow. II: Snow containing atmospheric aerosols," J. Atmos. Sci. **37**(12), 2734–2745 (1980).
80. J. Hansen and L. Nazarenko, "Soot climate forcing via snow and ice albedos," Proc. Natl. Acad. Sci. U. S. A. **101**(2), 423–428 (2004).
81. T. Grenfell and B. Light, "Spectral Albedo. Version 1.0 UCAR/NCAR - Earth Observing Laboratory", DOI: 10.5065/D6765CQ1 (2007).
82. D. Perovich, "Spectral Light Transmittance. Version 1.0 UCAR/NCAR - Earth Observing Laboratory", DOI: 10.5065/D6T1521W (2007).
83. G. F. Cox and W. F. Weeks, "Salinity variations in sea ice," J. Glaciol. **13**(67), 109–120 (1974).
84. N. Untersteiner, "Natural desalination and equilibrium salinity profile of perennial sea ice," J. Geophys. Res. **73**(4), 1251–1257 (1968).
85. M. Ardyna, C. J. Mundy, N. Mayot, L. C. Matthes, L. Oziel, C. Horvat, E. Leu, P. Assmy, V. Hill, P. A. Matrai, M. Gale, I. A. Melnikov, and K. R. Arrigo, "Under-Ice Phytoplankton Blooms: Shedding Light on the "Invisible" Part of Arctic Primary Production," Front. Mar. Sci. **7**, 1 (2020).
86. P. Massicotte, R. Amiraux, M.-P. Amyot, P. Archambault, M. Ardyna, L. Arnaud, L. Artigue, C. Aubry, P. Ayotte, and G. Bécu, "Green Edge ice camp campaigns: understanding the processes controlling the under-ice Arctic phytoplankton spring bloom," Earth Syst. Sci. Data **12**(1), 151–176 (2020).
87. P. Assmy, P. A. Dodd, and P. Duarte, *et al.*, "N-ICE2015 sea ice biogeochemistry," (2017).
88. D. K. Perovich, C. S. Roesler, and W. S. Pegau, "Variability in Arctic sea ice optical properties," J. Geophys. Res. Oceans **103**(C1), 1193–1208 (1998).
89. K. R. Arrigo, D. K. Perovich, R. S. Pickart, Z. W. Brown, G. L. Van Dijken, K. E. Lowry, M. M. Mills, M. A. Palmer, W. M. Balch, and F. Bahr, "Massive phytoplankton blooms under Arctic sea ice," Science **336**(6087), 1408 (2012).
90. K. Golden, "Brine percolation and the transport properties of sea ice," Ann. Glaciol. **33**, 28–36 (2001).
91. P. Popović, M. C. Silber, and D. S. Abbot, "Critical percolation threshold restricts late-summer Arctic sea ice melt pond coverage," J. Geophys. Res. Oceans **125**(8), e2019JC016029 (2020).
92. G. A. Schmidt, R. Ruedy, J. E. Hansen, I. Aleinov, N. Bell, M. Bauer, S. Bauer, B. Cairns, V. Canuto, and Y. Cheng, "Present-day atmospheric simulations using GISS ModelE: Comparison to in situ, satellite, and reanalysis data," J. Clim. **19**(2), 153–192 (2006).
93. Y. Hu and K. Stamnes, "An accurate parameterization of the radiative properties of water clouds suitable for use in climate models," J. Clim. **6**(4), 728–742 (1993).